Two-Line Planar Fluorescence for Temporally Resolved Temperature Imaging in a Reacting Supersonic Flow over a Body

J. M. Seitzman*, R. K. Hanson

High Temperature Gasdynamics Laboratory, Department of Mechanical Engineering, Stanford University, Stanford, CA 94305, USA
(Fax: +1-415/723-1748, e-mail: jms@navier.stanford.edu)

Abstract. An instantaneous temperature imaging technique for chemically reacting, supersonic flows over bodies is described and demonstrated in a $H_2/O_2/Ar$ shock tube flow ($M = 1.3$, 0.7 atm, 1760 K freestream). Based on a planar fluorescence measurement, the approach uses a two-line rotational population ratio to infer temperature. The measured 2-d temperature profiles qualitatively match the expected flowfield structure around the blunt body, and the temperature increase across the bow shock in a single-shot measurement agrees within 5–10% of the prediction of a 1-d shock analysis. The significant systematic error sources for the technique are detailed, and the random error effects associated with shot-noise-limited fluorescence images are statistically analyzed to identify transitions which minimize the temperature errors for instantaneous and average measurements. Even for average temperature measurements, the analysis predicts errors which can be as large as 5–10% when noisy fluorescence images are used in conjunction with low temperature sensitivity. In general, temperature errors can be reduced by increasing sensitivity, i.e., the energy separation of the two rotational levels, until the fluorescence shot-noise rises to a value of 30–50% within the temperature range of interest.

PACS: 07.20.Ka, 47.40.Ki, 47.70.Fw

Nonintrusive, planar imaging of temperature, a fundamental thermodynamic property, can play an important role in the study of chemically reacting supersonic flows. Along with the same basic insights provided by other flow visualization techniques [1], temperature imaging supplies quantitative measurements. One challenging application for temperature imaging is high enthalpy, compressible flow over a body. Such flows exhibit large variations in temperature, pressure (thus density) and velocity. The reactive nature of these flows range from complicated combustion processes to simple air chemistry. These supersonic reacting flows are of

current interest in SCRAMJET propulsion devices [2] and ram accelerators [3] for space launch systems.

For unsteady flow systems, complete characterization can require the application of a temporally resolved (instantaneous) temperature technique; this is true even for time-averaged measurements if the temperature is inferred from another parameter which has a nonlinear temperature dependence (as in the technique described here). Additionally, short test times and limited repetition rates at a number of flow facilities, e.g., many hypersonic and high enthalpy ground test sites, limit acquisition to a single image or to data sets too small for meaningful averaging.

Various optical techniques have been proposed for spatially and temporally resolved thermometry [4–6], and a few have been extended to imaging measurements [6–8]. For *instantaneous* two-dimensional imaging, Planar Laser-Induced Fluorescence (PLIF) is particularly attractive, owing to its excellent spatial resolution, high sensitivity and well-understood behavior. Two basic approaches have been demonstrated for PLIF temperature imaging. The first demonstration of instantaneous measurements [9] relied on a single fluorescence image, but required a constant mole fraction of the absorbing species and assumed temperature independent quenching cross-sections. More recently, this approach has been applied with some success to a nearly chemically frozen, high enthalpy, Mach 3 airflow over a sphere [10]. Though simple to implement, this technique is limited to a narrow range of flows.

The most general PLIF technique for instantaneous temperature imaging involves the ratio of two, nearly simultaneous images. In this approach, two laser sheets, each tuned to excite a transition with a different initial quantum energy level in the same molecular species, are passed through the same plane in the flow. The ratio of the fluorescence from the two sheets can then be related to a relative population ratio, and thus temperature, assuming Boltzmann statistics. This method has been applied to high-temperature mixing flowfields seeded with nitric oxide [11] and to atmospheric-pressure combustion flows using the hydroxyl radical [12, 13]. Because of their natural occurrence, NO and OH are attractive candidates for temperature mea-

---

* To whom all correspondence should be addressed

surements in applications involving high temperature air chemistry and hydrogen/hydrocarbon combustion, respectively. In addition, excitation/detection strategies which allow for efficient rejection of laser light scattering have been developed for both species. Thus, measurements can be quite close to solid surfaces.

Accurate instantaneous temperature imaging requires careful attention to potential error sources, both systematic and random. Errors in the fluorescence data are related to temperature errors by a measurement sensitivity. As explained below, the temperature sensitivity of the two-line technique depends on the energy spacing of the two initial levels. In most previous two-line temperature imaging, the tradeoff between sensitivity and the signal loss (thus increased noise) associated with large energy spacings was balanced by choosing two levels with a spacing comparable to the peak temperature in the flow. A more detailed approach for optimizing the energy difference has been presented for the case of single-point measurements in low temperature wind tunnels with two-photon-excited LIF of NO [14]. That work, based on a linear perturbation analysis and limited to high Signal-to-Noise Ratio measurements (SNR>100:1), however, failed to consider the true probability distributions associated with shot-noise-limited measurements.

Here, we describe instantaneous temperature images acquired in a high temperature, supersonic $H_2/O_2/Ar$ flow (1750 K, $M = 1.3$ freestream) over a blunt rectangular body. The temperature measurements were performed with the two-line fluorescence ratio technique and the OH radical. The significant systematic error sources, most of which have been analyzed previously, are summarized. A generalized analysis method for predicting the random error effects associated with shot-noise-limited fluorescence images is then presented. This statistical analysis is used to identify transitions which minimize the errors for both instantaneous and average temperature measurements.

1 Two-Line Temperature Imaging and Systematic Errors

As previously stated, the two-line technique involves two laser sheets, each tuned to excite a different initial quantum energy level, which pass through the same plane in the flow. The two laser sheets pass through this image plane with a relative delay that is long enough to prevent fluorescence from the first laser appearing on the second image, but short enough to effectively freeze the flow. The two images, one from each laser sheet, are acquired with a broadband detection scheme; emitted light is collected from the upper level directly produced by the laser, as well as from nearby levels populated indirectly by collisions. For weak (nonperturbing) laser pulses, the ratio R of the two fluorescence signals from a single flow volume is given by [7]

$$R = \frac{\eta_1 B_1 E_1}{\eta_2 B_2 E_2} \frac{g_1}{g_2} \frac{\phi_1}{\phi_2} \frac{f_1}{f_2},\qquad(1)$$

where for each image/absorbing level combination i: η_i is the collection efficiency of the camera optics and detector, B_i is the stimulated absorption coefficient, E_i is the laser energy fluence (e.g., W/cm^2), g_i is the overlap integral

between the laser and molecular absorption profiles, ϕ_i is the fluorescence yield, and f_i is the fractional population of the lower laser-coupled level in the absence of the laser field. Since the fluorescence ratio is independent of absorber number density, this approach is applicable to variable density flows, even in the presence of chemical reactions. Of course, a sufficient absorber number density must exist at a measurement point to produce a recordable signal.

Assuming the only temperature dependence in the fluorescence ratio comes from the relative populations in the absorbing levels, which in thermal equilibrium is governed by Boltzmann statistics, the fluorescence ratio can be converted to a temperature measurement by

$$T = \frac{-\Delta\varepsilon_{12}/k}{\ln(R/C) - \ln(E_1/E_2)},\qquad(2)$$

where C is a parameter which can be calculated or (more typically) treated as a calibration constant and $\Delta\varepsilon_{12}$ is the energy difference between the two lower, absorbing levels. If the lower levels of the two transitions differ only in rotational quantum number (N), the measurement is one of rotational temperature, which under most practical conditions can be considered to be in equilibrium with the translational temperature of the gas.

In the model presented above, simplifying assumptions are potential sources of systematic error. For example, (1) requires that fluorescence trapping (resonant absorption of the fluorescence by gas between the measurement plane and the detection system) is either negligible or identical for the two fluorescence signals. If both images are collected through the same or equivalent optical paths, potential trapping effects are minimized. In (2), the temperature dependence of the overlap integral and fluorescence yield ratios was also neglected. For at least two candidate PLIF tracer species, NO and OH, g_1/g_2 and ϕ_1/ϕ_2 have been shown to be temperature independent or to have a negligible temperature dependence if the transitions and calibration conditions are properly chosen [11, 13, 15, 16]. For example, although the fluorescence yield ϕ is known to be rotation-level dependent for OH, the temperature dependence of ϕ_1/ϕ_2 is small for OH at elevated temperatures (>1000 K) and for moderately high values of N [15].

Other potential sources of systematic error include pulse-to-pulse fluctuations in the calibration constant C, induced by shot-to-shot mode instability in the lasers' spectral profiles [11, 15]. When the calibration is in situ, this error is avoided. The laser energy ratio correction potentially requires single-shot monitoring of the laser sheet energy profiles, and negligible attenuation of the laser beams. Nonlinear averaging of temperature variations on a scale smaller than the finite spatial resolution of the image can also occur [11]. Another spatial effect is pixel-to-pixel mismatch between the cameras, which can be minimized with proper alignment and simple post-processing. Finally, the delay between the two laser pulses should be less than the relevant time scales of the flow, e.g., chemical reaction times and flow times for a fluid element to convect from one image resolution element to its neighbor.

2 Random Errors: Statistical Analysis

Although minimizing systematic errors is important, controlling random errors (noise) is vital in "single-shot" temperature imaging. Instantaneous PLIF imaging in high temperature flows is typically shot-noise-limited, with $2 < SNR < 30$. For high SNR fluorescence measurements, the random temperature error can be related to the noise in the ratio measurement through the local slope sensitivity,

$$\frac{dR/R}{dT/T} = \frac{1/SNR_R}{dT/T} = \frac{\Delta\varepsilon_{12}}{kT} , \qquad (3)$$

where the noise of the ratio measurement $1/SNR_R$ is typically assumed to be $(SNR_1^{-2} + SNR_2^{-2})^{1/2}$. With a high sensitivity $(\Delta\varepsilon_{12} \gg kT)$, the noise in the fluorescence ratio measurement results in small temperature errors. Increasing the energy spacing between the two initial levels will, however, tend to increase the shot-noise associated with the signal from the higher energy level, since high lying energy levels usually have lower populations.

While the optimum tradeoff can be calculated using a simple model like (3) for high SNR data [14], the nonlinear nature of ratio measurements and the temperature equation (2) requires that we consider the true probability distribution of shot-noise-limited signals for lower SNR images. For example, the logarithmic nature of the temperature equation (1) allows a fraction of measurements in the wings of a noise distribution to have an excessive impact on the inferred temperature. This is illustrated in Fig. 1, which shows the error in the normalized temperature $T/(\Delta\varepsilon_{12}/k)$ one would infer with various fractional deviations in the normalized fluorescence ratio R/C. The increased slope of the logarithm function at high values of R/C causes amplification of the measurement noise for large positive errors $(R_{meas} > R_{expected})$.

The statistical noise in the ratio measurement can be predicted by calculating the probability distribution for the individual fluorescence signals. For signals dominated by shot-noise, the probability of an integrating detector recording k

counts when the expected (average) value is $K(\equiv \langle k \rangle)$ is given by a Poisson distribution, $P(k) = (K^k/k!)e^{-K}$. The statistical moments, e.g., mean, standard deviation and skewness (third moment normalized by the standard deviation), associated with the temperature measurement can then be compiled from the probability of measuring a given two-line fluorescence ratio $R = k_1/k_2$, which corresponds to a given temperature through the temperature relation (2). For example, the mean temperature $\langle T(R) \rangle$ calculated by first converting the instantaneous fluorescence ratios to instantaneous temperature data and then averaging is given by

$$\langle T(R) \rangle = \sum_{k_1=0}^{\infty} \sum_{k_2=0}^{\infty} P(k_1)\, P(k_2) \frac{-\Delta\varepsilon_{12}}{\ln[(k_1/k_2)/C']} , \qquad (4)$$

where the laser energy term has been incorporated into C'. Similarly, one can average the instantaneous ratio measurements before converting to temperature and obtain

$$\langle T(R) \rangle = \frac{-\Delta\varepsilon_{12}}{\ln\left\{\left[\sum_{k_1=0}^{\infty} \sum_{k_2=0}^{\infty} P(k_1)\, P(k_2) k_1/k_2\right]\middle/ C'\right\}} . \qquad (5)$$

The mean temperature can also be calculated by averaging the instantaneous images before taking the ratio; that approach is limited, however, to completely steady or repeatable flows. The error in the measured mean temperature is then the difference between it and the true average temperature T, denoted here as the fractional mean deviation ΔT, e.g., $\Delta\langle T(R) \rangle = (\langle T(R) \rangle) - T)/T$.

The statistical results of an example calculation are summarized in Fig. 2, which shows the probability distribution that is predicted for temperature measurements at a fixed temperature and energy spacing, $T/(\Delta\varepsilon_{12}/k) = 0.77$ (e.g., measurement of a 2000 K flow with a 2600 K separation between the initial energy levels). Thus, Fig. 2 represents the distribution of temperatures one would obtain either (i) at a given pixel for a large image set in a steady flow, or (ii) within a large uniform region in a single instantaneous temperature image from a (possibly) unsteady flow. In the
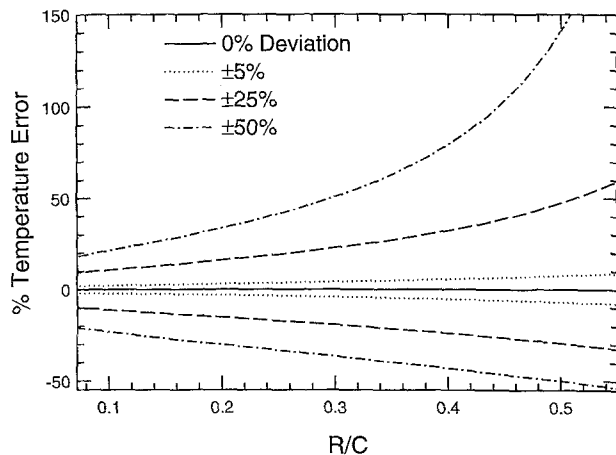

Fig. 1. Temperature errors associated with fixed deviations from the expected, normalized temperature $T/(\Delta\varepsilon_{12}/k)$ caused by various fractional deviations in the normalized fluorescence ratio R/C; positive temperature errors result from positive deviations in R ($R_{meas} > R_{expected}$)
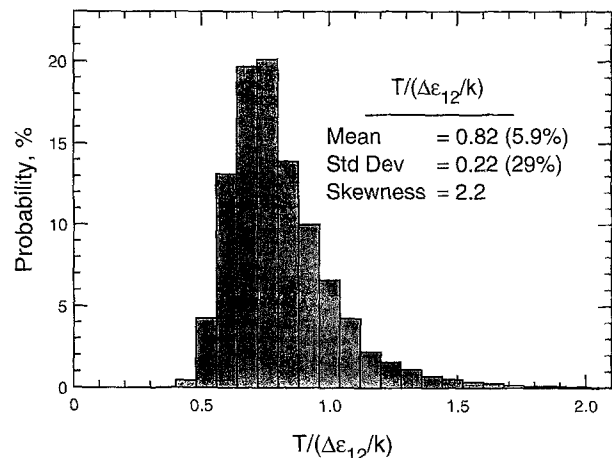

Fig. 2. Probability distribution of temperatures that would be recorded for a fixed temperature to energy spacing ratio $T/(\Delta\varepsilon_{12}/k)$ of 0.77 and with the ratio of two signals, each having a SNR of 5:1; temperatures outside a range of 0–2 normalized energy spacings $(\Delta\varepsilon_{12}/k)$ were omitted from the statistical moment calculations

calculation, both detectors were chosen to have a SNR of 5:1 ($\pm 20\%$ noise). Since the possible number of distinct ratios associated with these low signal levels is small, the probability distribution is shown in a discrete form. Also included in Fig. 2 are the values of the first three moments of the temperature distribution.

The asymmetry evident in the probability distribution results from the nonlinear (logarithmic) sensitivity described above, as well as the asymmetry of the statistical distribution of fluorescence ratios (not shown). The temperature asymmetry, associated with the positive skewness value of 2.2, causes the error in the mean temperature measurement ($\Delta\langle T(R)\rangle = 5.9\%$) and increases the random error by a factor of 1.4 compared to the result of the simple analysis (3). Only normalized temperatures in a range of 0–2 (0–5200 K for a nominal 2000 K measurement) were included in the statistics. This is analogous to the type of thresholding that might be applied to statistical interpretation of noisy data. The importance of the wings of the probability distribution are even more evident if we consider the moment values for all positive temperatures. While 0.4% of the possible values have a normalized temperature greater than 2, including these increases the standard deviation from 29% to 47%. A smaller change (5.9% to 6.5%) occurs for the mean deviation. Thus with a priori information on the range of expected temperatures, data thresholding can be used to reduce the statistical errors.

3 Blunt Body Experiment

3.1 Transition Selection

The statistical analysis described above was performed for PLIF measurements of OH across the temperature range expected in our blunt body flow, 800–2300 K, as a guide in choosing the optimum transition pair. The OH transitions were selected from the $A^2\Sigma^+ \leftarrow X^2\Pi$ (1, 0) band, which allows for nonresonant fluorescence detection and suppression of elastic laser scattering. However, the general approach, as well as some of the overall conclusions presented below, are not limited to this transition system or to the OH molecule.

In general, the statistical analysis of the proper transition pair would involve studying transitions with different lower and higher initial energy levels (or different rotational quantum numbers N_{low} and N_{high}), and the maximum transition strength B. In addition to the random error effects, however, the systematic error sources, e.g., the temperature dependence of the fluorescence yield ratio and laser absorption, previously described, must also be considered in the transition choice. For these reasons, the $R_2(5)$ line was chosen for the lower energy transition; $N_{low} = 5$ was picked to restrict the temperature dependence of the fluorescence yield ratio, and the R-branch transition (as opposed to the stronger Q-branch) was used to reduce laser absorption.

For the higher energy transition, N_{high} was varied from 10–14 ($\Delta\varepsilon_{12}/k$ from 2100–4700 K), and since the absorption coefficient is lower for these more poorly populated levels, strong Q-branch transitions were selected. The calculated fluorescence signals are fixed by the SNR in the

freestream for the $R_2(5)$ image; the value expected from previous measurements is ~ 4.2 [15]. The signal variation across the flowfield was modeled as follows. In this flow, the fluorescence scales primarily as OH mole fraction (not density) and Boltzmann population. Since the OH mole fraction is expected to vary by less than $\pm 20\%$, the signal was assumed to vary strictly with temperature, according to the Boltzmann population. With this model for the N_{low} signal, the N_{high} signal is given by (2) and $C' \cong 1.3(B_{high}/B_{low})(2N_{high}+1)/(2N_{low}+1)$, with the value of 1.3 set by the experimental conditions, e.g., laser energy.

Figure 3 shows calculated fractional mean Δ and standard deviations σ, normalized by the true temperature, for $N_{high} = 10$–13. The errors associated with both methods of obtaining the mean temperature, (4) and (5), are shown. To simulate the actual data reduction process, in which obviously erroneous measurements are excluded, temperatures outside a range of 400–4600 K (from one-half of the minimum to twice the maximum expected temperature) were omitted from the statistical calculations, and the probability of omission is also presented. Calculations are shown for the expected $R_2(5)$ freestream SNR (~ 4.2) and a value twice this (~ 8.5).

As shown in Fig. 3a, b, the average temperature measurements can differ from the actual mean temperature by up to 7% for our conditions. Except at the low temperatures, averaging the instantaneous ratios (Fig. 3b) is more accurate, $\Delta T(\langle R\rangle) < 5\%$, than averaging the instantaneous temperatures (Fig. 3a). Calculations (not shown) at a lower SNR value of 3 produce average temperatures with errors from 5 to 10%. Thus, without the higher sensitivity advantages described below, noisy fluorescence data can cause significant errors even in average temperature measurements. With a
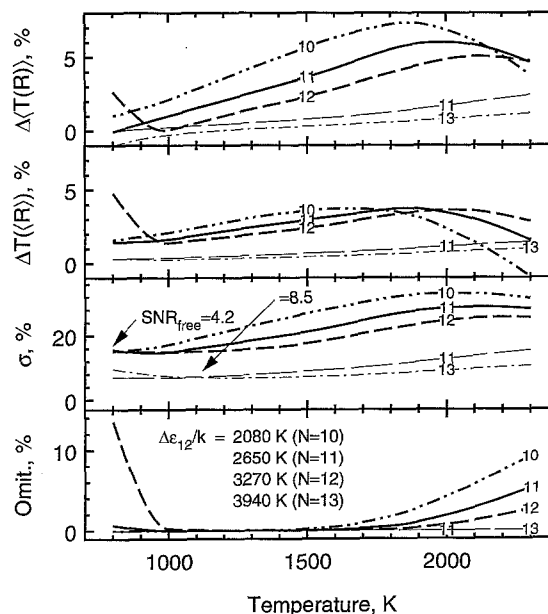

Fig. 3. Statistical temperature errors (mean deviations, standard deviations and probability of measuring temperatures outside the 400–4600 K range) associated with shot-noise-limited fluorescence ratios using the $R_2(5)$ line and Q_2-branch lines with various N (the energy spacing for each N is listed); calculations are shown for a freestream SNR in the $R_2(5)$ image of 4.2 (*bold lines*) and 8.5

factor of two improvement in the expected $R_1(5)$ SNR, i.e., a 4-fold increase in signal, the error in the measured average temperature is limited to 2%. Again, the error in the average temperature results from the nonlinear nature of the two-line ratio technique, which produces asymmetric probability distributions. For the conditions of Fig. 3, the skewness of the temperature distributions (not shown) varies between 0.5–1.5 and 0.2–0.8 for the low and high SNR cases, respectively.

The normalized uncertainties (Fig. 3c) for the SNR = 4.2 case vary between roughly 15% and 30%, with the larger values of N_{high} (thus better sensitivity) producing the lowest random errors. While temperatures measured with larger N_{high} values are less noisy, the number of measurements which must be excluded at low temperatures increases (Fig. 3d). The opposite is true at high temperatures, where the increased sensitivity outweighs the worsening fluorescence noise. As with the mean deviations, an increase in the freestream SNR to 8.5 reduces the standard deviations to as low as 7%. Additionally, the fraction of omitted data is below 1.5% for all the high SNR cases except $N_{high} = 14$ (not shown) below 1000 K.

For the estimated conditions of our blunt body flow, the $Q_2(11)$ line has the least overall temperature error. Combined with the $R_2(5)$ line, this gives an energy spacing of 2650 K, or a sensitivity factor of 1.15–3 for our temperature range. Increasing N_{high} to 12 improves σ by only a few percent, but drastically increases the probability of omitting measurements below 1000 K. If we could increase the freestream signal by a factor of four, the $Q_2(13)$ line ($\Delta\varepsilon_{12}/k = 3940$ K) would be a better choice. The $Q_2(13)$ line has a SNR of only 2.2 at 800 K, but the high sensitivity (4.9) limits the temperature uncertainty to 10% and the fraction of omitted data is only 0.7%. Similar calculations for combustion gases and high enthalpy flows lead us to the following conclusion: for measurements over a given temperature range, the energy spacing (sensitivity) of the line pair should be increased until the SNR in an image falls to a value of roughly 2–3 within the considered range. Until this point, the benefits of the increased sensitivity outweigh noise induced by the larger signal loss.

3.2 Experiment

The experimental arrangement used to obtain the temperature images is described in detail elsewhere [15]. In brief, two coplanar sheets of pulsed laser light from two excimer-pumped, frequency-doubled tunable dye lasers were used to induce fluorescence from OH produced in a shock-heated flow (1.0 km/s, 1760 K, 0.7 atm, $M = 1.3$ free stream) over a thick 2-d rectangular plate (8 mm × 70 mm) with a flat nose. As suggested by the shot-noise analysis, fluorescence images were acquired by exciting the $Q_2(11)$ (~285 nm) and $R_2(5)$ (~282 nm) transitions in the $A^2\Sigma^+ \leftarrow X^2\Pi$ (1, 0) band of OH. The OH was formed, primarily in the supersonic freestream, by reactions in the original mixture of 3% H_2 and 6% O_2 diluted in an Ar bath. From a chemical kinetics analysis [15], the freestream consists of 0.37% OH, 4.2% O_2, 2.1% H_2O, 1% O, 0.83% H, and 0.24% H_2. Both laser beams were expanded into collimated sheets using the same set of optics. The 60 mm × 300 μm laser sheets arrived at the entrance window of the 3 × 3 in. square cross-section shock tube 100 ns apart and with energies of 250–500 μJ in each sheet.

The resulting broadband fluorescence was imaged by two identical detectors (f/4.5 UV Nikkor camera lens; 18 mm, single-microchannel-plate intensifier with ~100 ns gate; fiberoptic coupling to a cooled 384 × 578 pixel Princeton Instruments CCD camera) located on opposite sides of the flow facility. A combination of longpass and bandpass optical filters were placed in front of the lenses to detect the (1,1) and (0,0) band fluorescence in the 305–320 nm range while removing laser scattering, e.g., from the laser sheet hitting the blunt body, and visible emission from the bright shock. Each camera system integrated the fluorescence signal induced from only one of the lasers. The cameras recorded fluorescence from a region starting at the laser entrance window and extending 30 mm into the shock tube, and 45 mm along the flow.

The field viewed by each camera was carefully adjusted such that pixel-to-pixel alignment errors were less than 1–2 pixels (78–156 μm) across the images. After the image corrections (see below), each image was pixel-binned 2 × 2); thus temperature errors associated with pixel mismatch are generally not significant. The temporal separation of the laser pulses results in a spatial blurring of ~100 μm, which is less than the limited spatial resolution of the intensifiers (150–200 μm) and less than the thickness of the laser sheet (300 μm). The fluorescence images were corrected for dark and background signal, laser scattering, and nonuniform pixel-to-pixel responsivity. Also included in the image corrections were data from single-shot laser monitors, which recorded the individual laser sheet energy and spectral profiles. The shot-to-shot laser energy profile fluctuations were nearly 10% (excluding long term drift, >1 h, and the noise in the single-shot measurement of the profiles was approximately 1–2%. Thus the residual temperature error after correction for the energy ratio E_1/E_2 (on a pixel-by-pixel basis) is less than 2% throughout the flow.

3.3 Results

Figure 4 shows an instantaneous temperature record of the flow over the rectangular body. The temperatures in this image were calibrated with the known freestream temperature (1760 K); the resulting temperature scale is included at the bottom of the figure. As expected, the image shows a temperature increase across the stationary, detached two-dimensional bow shock upstream of the body [17]. After the bow shock, the flow at the bottom of the image, which is approximately the centerline of the blunt body, must slow down, approaching the gas stagnation temperature. Figure 4 shows this temperature rise, with the gas temperature starting at the freestream value of 1760 K and increasing, as the flow approaches the face of the body, to a spatially averaged value of 2730 K. This is slightly higher than the stagnation temperature of ~2600 K from an ideal gas calculation.

The temperature field also contains a cold expansion zone (dark region) just downstream of the plate's leading edge, with a minimum measured temperature of 850 K, and then a recovery of the static temperature in the boundary layer
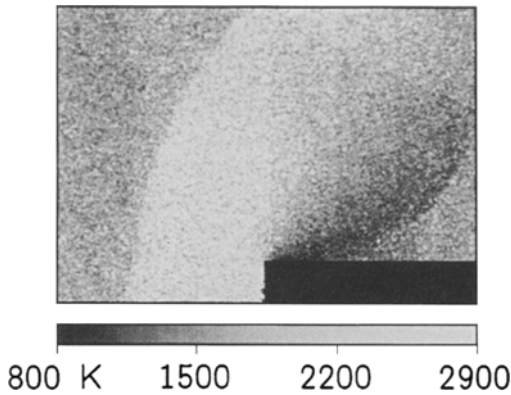
Fig. 4. Instantaneous OH temperature image (30 mm × 45 mm) acquired with the $Q_2(11)/R_2(5)$ line pair of the flow (*left* to *right*) over a blunt rectangular body (*bottom right*), with freestream conditions of Mach 1.3, 0.7 atm and 1760 K; half of the 8 mm thick plate (*bottom right*) is within the imaged region, while the remainder falls below the image

reattachment shock downstream of the expansion zone. At the top and right of the image, a reflection of the bow shock off the laser entrance window can be seen. Rejection of laser scattering was sufficient to allow temperature measurements within 300 μm of the body surface, even with the laser sheet striking the top of the body.

A more detailed look at the temperature field is shown in Fig. 5, a horizontal cut through the flow, 3 mm above the flat plate. The increase in temperature across the bow shock, followed by the temperature drop in the expansion around the recirculation zone and the thermal recovery across the reattachment shock are clearly evident. At the height of the horizontal cut, the shock angle is 85°; from an ideal gas, 1-d oblique shock analysis, this would suggest a temperature just across the shock of 2220 K (and a pressure of 1.2 atm). From the running average shown in Fig. 5, the measured temperature is roughly 2450 K, 10% above the oblique shock calculation. We expect a 5% high measurement error because of the nonlinear sensitivity (Fig. 3); the remainder may result from other systematic
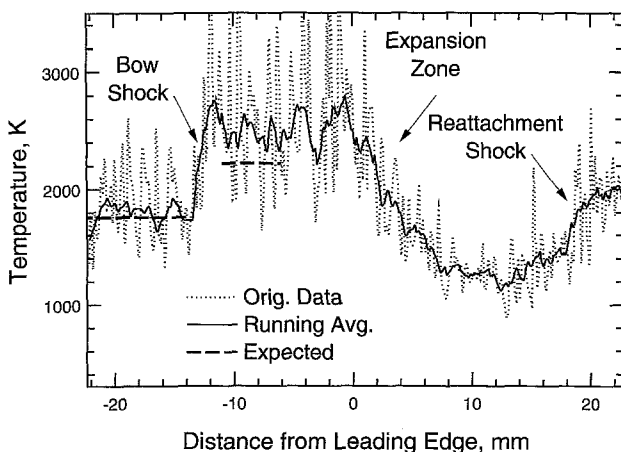
errors or the simplicity of our analysis. As predicted by the results of Fig. 3, the temperature uncertainty is greatest at high temperatures, with nearly the same value in the freestream and just downstream of the bow shock. In the freestream, the measured uncertainty is roughly 21% of the average (±400 K), slightly less than the predicted value of 25%. After the bow shock, the 25% measured error is close to the predicted value of 27%.

4 Conclusions

In summary, we have demonstrated a temperature imaging technique for high temperature, supersonic flows over bodies, based on a fluorescence measurement of a two-line rotational population ratio. In most cases, the measured rotational temperature should be in equilibrium with the translational temperature, except in thin shock waves. While this particular demonstration used the naturally occurring combustion radical OH, the technique is equally applicable for a species like NO [11], which can be seeded into the flow or occurs naturally in high temperature air streams. Rejection of laser scattering was sufficient to allow temperature measurements within 300 μm of the body surface, even with the laser sheet striking the top of the body. The temperature images qualitatively match the expected flowfield structure around the blunt body used here, and the temperature increase across the bow shock agrees within 5–10% of the prediction of a 1-d oblique shock analysis.

The statistical analysis of the temperature errors for low SNR fluorescence imaging accounts for the tradeoff between temperature sensitivity and signal loss and is useful for choosing a transition energy spacing that minimizes the errors. The calculated temperature errors result from the skewed temperature probability distribution associated with shot-noise-limited statistics and the nonlinear relationship between the fluorescence ratio and temperature. Even for average temperature measurements, the model predicts errors which can be as large as 5–10% if low SNR fluorescence images are used in conjunction with low sensitivities ($\Delta \varepsilon_{12}/kT$ below 1–2). At most of the conditions considered here, more accurate mean temperatures are obtained by averaging the fluorescence ratios before converting to temperature, as opposed to converting the instantaneous ratios to temperature and then averaging. In addition, data thresholding can be used to reduce the errors caused by the wings of the asymmetric probability distribution.

In general, temperature errors can be reduced by increasing sensitivity, e.g., increasing the energy of the higher initial rotational level, until the SNR drops to a value near 2–3 within the temperature range of interest. For the current conditions, the highest single-shot temperature uncertainties were near ±25%, in good agreement with the model. With simply a factor of four improvement in the laser energies used here (from 250–500 μJ to 1–2 mJ), the temperature uncertainty would be improved to a value below ±10%. These laser energies are easily attainable with commercially available laser systems and are below the levels at which nonlinear (saturation) behavior of the fluorescence signals must be considered.

Fig. 5. Horizontal cut (3 mm above the body) through the temperature image of Fig. 4; both the temperature data and a 1 mm running average are shown

References

1. R.K. Hanson: *21st Symp. (Int'l) on Combustion* (The Combustion Institute, Pittsburgh, PA 1987) pp. 1677–1691
2. F.S. Billig: AIAA 92-0001, AIAA 30th Aerospace Sciences Meeting, Reno (1992)
3. A. Hertzberg, A.P. Bruckner, D.W. Bodganoff: AIAA J. **26**, 195 (1988)
4. M.L. Elder, J.D. Winefordner: Prog. Anal. Atom. Spectrosc. **6**, 293 (1983)
5. B. Yip, P.M. Danehy, R.K. Hanson: Opt. Lett. **17**, 751 (1992)
6. N.M. Laurendeau: Prog. Energ. Comb. Sci. **14**, 147 (1988)
7. R.K. Hanson, J.M. Seitzman, P.H. Paul: Appl. Phys. B **50**, 441 (1990)
8. P. Ewart, M. Kaczmarek: Appl. Opt. **30**, 3996 (1991)
9. J.M. Seitzman, G. Kychakoff, R.K. Hanson: Opt. Lett. **10**, 439 (1985)
10. M. Allen, J.F. Cronin, S.J. Davis, R.R. Foutter, T.E. Parker, W.G. Reinecke, D.M. Sonnenfroh: AIAA 93-0092, AIAA 31st Aerospace Sciences Meeting, Reno (1993)
11. B.K. McMillin, J.L. Palmer, R.K. Hanson: Appl. Opt. (1993, in press)
12. M. Allen, S. Davis, K. Donohue: AIAA 90-2383, AIAA/SAE/ASME/ASEE 26th Joint Propulsion Conference, Orlando (1990)
13. P.H. Paul, U.E. Meier, R.K. Hanson: AIAA 91-0459, AIAA 29th Aerospace Sciences Meeting, Reno (1991)
14. R.L. McKenzie, K.P Gross: Appl. Opt. **20**, 2153 (1981)
15. J.M. Seitzman, R.K. Hanson, P.A. DeBarber, C.F. Hess: Appl. Opt. (1993, in press)
16. R. Cattolica: Appl. Opt. **20**, 1156 (1981)
17. W.A. Mair: Philos. Mag. **43**, 695 (1952)